Research Article Vol. 32, No. 8 / 8 Apr 2024 / Optics Express 14261
Optics EXPRESS

Tamm and surface plasmon hybrid modes in anisotropic graphene-photonic-crystal structure for hemoglobin detection

MD. MAHBUB HOSSAIN AND MUHAMMAD ANISUZZAMAN TALUKDER*

Department of Electrical and Electronic Engineering, Bangladesh University of Engineering and Technology, Dhaka 1205, Bangladesh
*anis@eee.buet.ac.bd

Abstract: We propose Tamm plasmon (TP) and surface plasmon (SP) hybrid modes for hemoglobin (Hb) detection in anisotropic graphene-photonic-crystal (GPC) structures. The proposed GPC sensor shows polarization-dependent responses due to the in-plane anisotropic property. The reflection profiles of the proposed sensor exhibit two reflectivity minima due to the simultaneous excitation of TP and SP modes. When used to detect Hb, the TP mode offers a greater figure-of-merit (FoM) than the SP mode. Using a Fourier mode spectral analysis, we observe energy coupling from the TP to the SP mode when the incident light's polarization changes, providing an option to enhance the sensor's sensitivity. We propose a double dips method (DDM) to detect Hb based on the simultaneous excitation of TP and SP modes. Using DDM, the proposed sensor offers a maximum sensitivity of 314.5 degrees/RIU and a FoM of 1746 RIU^{-1} when the Hb level is 189 g/L. The proposed anisotropic GPC sensor offers possible applications for highly sensitive bio-molecule detection with high FoM.

1. Introduction

In surface plasmon resonance (SPR), transverse magnetic (TM) surface waves propagate at the dielectric-metal interface. Such SPR resonances show a broad reflected light intensity profile (*R*-profile) due to scattering and absorption losses in the noble metal [1]. Therefore, SPR optical sensors are limited in their performances and further development. Using two-dimensional (2-D) graphene in SPR sensors is promising to enhance performance. However, the light absorption by a graphene monolayer is only 2.3%, insufficient for optical sensing and modulation [2]. Increasing the graphene layer number can increase the light absorption and the SPR sensor's sensitivity. However, the full-width at half-maximum (FWHM) of *R*-profiles broaden when the graphene layer number increases [3], limiting graphene's applications in plasmonic sensors [4].

Different research groups have proposed graphene-photonic-crystal (GPC) structures to increase the light-graphene layer interaction [1,5–7]. GPCs, generally known as an artificial periodic array structure formed by graphene, dielectrics, and photonic crystals (PCs), are a form of photonic devices created through intermittent preparation of dielectric layers of different refractive indices [8]. Structures based on multi-layer dielectric on monolayer graphene have been explored previously [9,10]. The graphene monolayer in a GPC can enhance the photon absorption by Bragg fluctuation, and therefore, the light-graphene interaction [4]. GPCs are suitable for numerous sensing applications due to their fast response time and ultra-high sensitivity [11]. In addition, the electromagnetic wave propagation in GPCs can be controlled by exploiting the structure's photonic bandgap (PBG) [12].

GPC structures have applications in optical modulators, polarizers, filters, and biosensors [13]. Surface plasmons (SPs) can be excited in GPCs with significant photon absorption, although SPs suffer scattering losses in GPCs [14]. GPCs also show properties of hyperbolic metamaterials

#514215 https://doi.org/10.1364/OE.514215
Journal © 2024 Received 23 Nov 2023; revised 23 Jan 2024; accepted 20 Mar 2024; published 3 Apr 2024

Optics EXPRESS

and support the excitation of Tamm plasmons (TPs), critical coupling, and negative refraction [15–20]. TPs are surface modes excited between metal and distributed Bragg reflector (DBR) [21]. TPs can be stimulated directly by the TM or transverse electric (TE)-polarized incident light, and there is no need for dispersion regulation like exciting SPs. The *R*-profile of TPs is narrower than SPs [7]. In addition, TPs show low absorption loss and high quality factor, which is appropriate for optical modulation and sensing [22]. We need high quality factors for optical sensing as it improves the detection accuracy and signal-to-noise ratio.

Hybrid TP-SP modes can be excited in a metal-GPC structure [23]. The TP mode is excited at the metal-GPC interface, while the SP mode is excited at the metal-sensing layer interface. As a result, an anti-crossing effect is observed on their dispersion relation [23]. The anti-crossing effect alters the hybrid TP-SP plasmonic modes' dispersion properties and decreases the SP mode's absorption losses. Therefore, the *R*-profile due to the excitation of hybrid TP-SP modes becomes narrower than the traditional SPR. The anti-crossing effect shows a coupling state between TP and SP, allowing energy exchange between these modes [24].

Recently, different research groups have proposed TP-based refractive index and temperature sensors [7,25,26]. A graphene-porous silicon PC has been proposed, where figure-of-merit (FoM) and sensitivity are controlled by varying the incident light angle and the porosity and thicknesses of silicon layers [27]. Also, asymmetric graphene-DBR has been used to create TP modes, and the effects of the incident light's polarization on sensor performances have been investigated [28]. In contrast, a refractive index sensor containing GPCs has been proposed as a defect layer [7]. However, the proposed refractive index sensor is polarization and phase-insensitive. Recently, a terahertz (THz) graphene-DBR refractive index sensor has been proposed where sensor performances are phase and polarization-dependent [29]. THz frequency cannot be used for complex bio-molecule detection due to non-ionizing behavior and low photonic energy radiation [30]. Besides, TP and SP modes can be combined to improve the sensor performances in the optical wavelength region [31].

Hemoglobin (Hb) is an essential part of blood found in the red blood cell (RBC). The oxygen supply to tissues depends on blood's Hb levels, and a variation in the Hb level causes health concerns [32]. Normal blood Hb levels are 120 to 160 g/L for females and 140 to 180 g/L for males [33]. The refractive index of blood changes by 0.001 unit (RIU) when the Hb level increases by 6.1025 g/L [33]. Heparin is widely used to determine the Hb level from RBC, requiring extensive pre-processing [34]. Heparin-based Hb level detection suffers measurement errors. A whispering gallery-based optical method has been used to detect the Hb level, although the sensitivity of this sensor is low [33]. In addition, a graphene-based SPR sensor has recently been proposed for Hb detection, with the sensitivity fluctuating with the Hb level [34].

This work proposes GPC-based TP-SP hybrid modes for Hb detection in the visible wavelength region. We have optimized the silver (Ag) layer thickness and the number of the unit cell (N) of GPCs, considering the minimum R and FWHM values. The energy coupling from TP to SP mode has been determined using the Fourier mode spectral analysis (FMSA). We show anti-crossing effects between TP and SP modes for the incident light's different polarization angles (φ). We use Barer's analytical model to calculate the optical properties of Hb in blood. The sensor's change of resonance angle ($\Delta\theta_r$) and FWHM for both TP and SP modes are calculated using the finite difference time domain (FDTD)-based angular interrogation method. In addition, we apply the double-dips method (DDM) to determine the sensitivity (S) and FoM. The proposed sensor shows energy coupling from TP to SP modes, helping improve the sensitivity for Hb detection.

The rest of the paper is organized as follows: Sec. 2 presents and discusses the proposed sensor structure and optimization. Section 2 discusses the anti-crossing effect between TP and SP modes and the simulation approaches. Section 3 presents the analytical models applied to investigate the optical properties of different materials and discusses the TP resonance mode

Optics EXPRESS

identification and the energy coupling from TP to SP modes. We show and discuss the calculated sensor performances in Sec. 4. Finally, we conclude the findings in Sec. 5.

2. Proposed sensor

2.1. Configuration

Figure 1 illustrates the proposed anisotropic GPC TP-SP hybrid Hb detection sensor. The graphene-based PC material layers are stacked on the BK7 prism substrate. The GPC comprises consecutive layers of graphene, SiO_2, and TiO_2 with thicknesses 1.02 nm, 110 nm, and 70 nm, respectively. The GPC structure is similar to a DBR structure [35]. Graphene monolayer thickness (t_g) is 0.34 nm. In the proposed sensor, we use three graphene monolayers ($3t_g$). SiO_2 and TiO_2 thicknesses are calculated by $d_s = \lambda/4n_s$ and $d_t = \lambda/4n_t$, where λ is the operating wavelength and n_s and n_t are the refractive indices of SiO_2 and TiO_2, respectively [7]. We have set $\lambda = 633$ nm as the operating wavelength, which is frequently used in SPR-based experiments [36]. SiO_2 and TiO_2 layers are chosen for wide PBG due to their significant refractive index contrast [1].

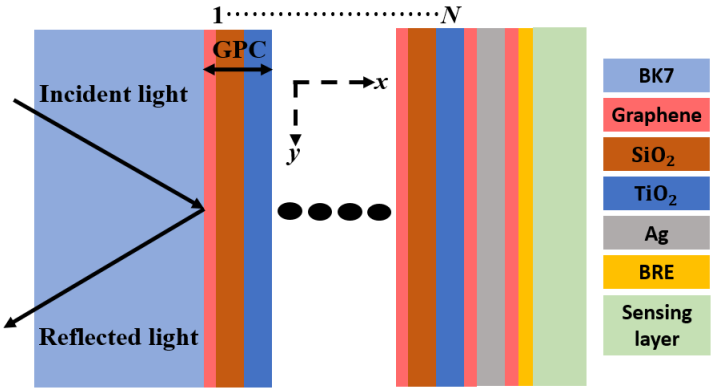

Fig. 1. Schematic illustration of the proposed anisotropic GPC-based TP and SP hybrid mode Hb detection sensor.

GPC is a periodic structure with a periodicity of 181.02 nm. The number of periods (N) is optimized as 9 for the minimum R value. At the top of the last period, we place another graphene layer with $3t_g$ thickness as the termination layer. The terminating graphene layer reduces the scattering loss of the SP mode [37]. Also, the graphene termination layer helps the Ag layer avoid oxidation. Followed by the graphene termination layer, the Ag layer has an optimized thickness (d_{Ag}) of 60 nm, which determines the strength of interaction between TP and SP modes in the sensing layer. Therefore, d_{Ag} plays a crucial role in the TP-SP mode coupling [26].

As Hb is a bio-marker of several diseases, fast and sensitive Hb detection is crucial. The human blood serum contains Hb as a sensing element that can flow on the top of the sensor surface by a flow channel [38]. We will need to bind Hb to immobilized antibodies on the graphene surface. Graphene has a rich π-π structure, which can immobilize antibodies like antibody-enzyme complex (AEC) [39]. We use a 20-nm AEC layer on the terminating graphene layer as the bio-recognition element (BRE) AEC to detect Hb in human blood. AEC will capture specific Hb present in the sample.

We have used the optimum thicknesses for different layers. The proposed sensor structure is planar, and using present-day fabrication technologies, the fabrication of the proposed structure is not complex. In practice, the graphene layer can be deposited on the prism or GPC by dissolving atomic carbon in a vacuum using high temperature [40]. Dielectric materials can be grown on

Optics EXPRESS

each other using evaporation techniques [41]. A glass flow cell can be used to inject analytes into the sensor [42].

2.2. Optimization of sensor structure

The Ag metal layer thickness and the GPC unit cell number N will critically affect the overall performance of the proposed sensor. Therefore, optimizing the proposed sensor's structural parameters is crucial for the best response. We have optimized d_{Ag} using the approach discussed in Ref. [43]. In particular, we examine the effect of d_{Ag} and the variation of N on R-profiles as a function of the incidence angle (θ_i). The optimization of d_{Ag} and N depends on the minimum reflected light intensity (R_{min}) and FWHM of the R-profile. While R_{min} occurs when the light absorption is maximum on the sensor surface, the FWHM represents the loss in the metal layer. Therefore, both R_{min} and FWHM are crucial for the sensitivity enhancement of a sensor, and an optimized d_{Ag} and N should produce both R_{min} and FWHM as small as possible. Here, we consider both resonances of TP and SP modes when optimizing d_{Ag} and N.

To optimize N, we vary it while keeping the layer thicknesses fixed. Here, we use sensing layer refractive index $n_{Hb} = 1.32919$ and $d_{Ag} = 60$ nm. Figure 2(a) shows R-profiles against θ_i for different N. We find two separate R minimum values. The first dip at ~57.52° is due to the excitation of TP between Ag and GPC, whereas the second dip at ~63.97° is due to the excitation of SP at the Ag-sensing layer interface. A detailed explanation of the identification of TP and SP modes is given in Sec. 3.2. We find that R_{min} and FWHM are minimum for the SP mode when $N = 9$. However, the TP mode shows a minimum R_{min} and FWHM when $N = 5$. When N increases from 5 to 9, R_{min} due to the TP mode increases from 0.2258 to 0.2718, indicating an absorption decrease of the incident light. Simultaneously, the R_{min} due to the SP mode decreases from 0.0490 to 0.0029, indicating an absorption increase of the incident light. We choose $N = 9$ for the proposed sensor.

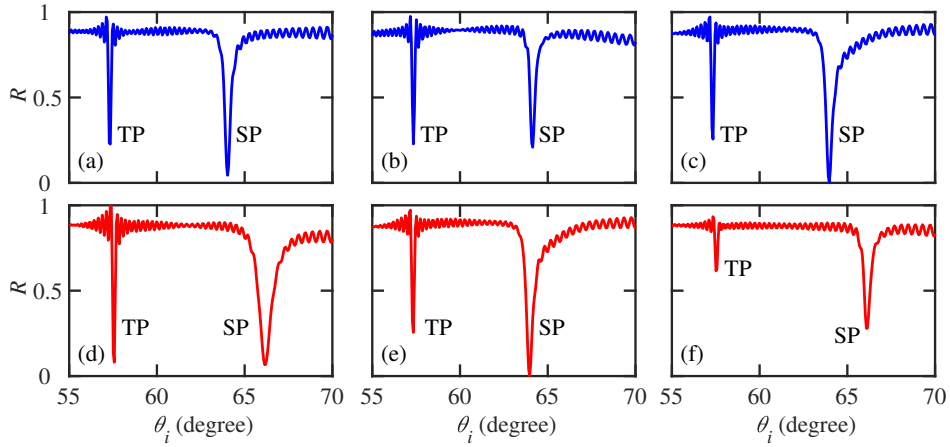

Fig. 2. R-profiles of the proposed sensor with the GPC unit cell number (a) $N = 5$, (b) $N = 7$, and (c) $N = 9$, when $d_{Ag} = 60$ nm. R-profiles of the proposed sensor with the Ag layer thickness (d) $d_{Ag} = 50$ nm, (e) $d_{Ag} = 60$ nm, and (f) $d_{Ag} = 70$ nm, when $N = 9$. In each case, $n_{Hb} = 1.32919$, and $\lambda = 633$ nm.

Next, we optimize d_{Ag} from calculations shown in Fig. 2(d)-(f). We change d_{Ag} while the other layer thicknesses are fixed, and $N = 9$. When $d_{Ag} = 60$ nm, both R_{min} and FWHM show minimum values for the SP mode. However, the TP mode shows minimum value when $d_{Ag} = 50$ nm. Increasing d_{Ag} from 50 nm to 60 nm, the FWHM becomes narrower for both SP and TP modes. Furthermore, when $d_{Ag} = 70$ nm, the R value increases for both resonances. When

Optics EXPRESS

d_{Ag} increases from 50 nm to 60 nm, R_{min} due to the TP mode increases from 0.088 to 0.2818, indicating an absorption decrease of the incident light. Simultaneously, R_{min} due to the SP mode decreases from 0.076 to 0.0029, indicating an absorption increase of the incident light.

2.3. Anti-crossing behavior

The proposed sensor's energy band can be altered using the anti-crossing effect between hybrid TP-SP modes [44]. The difference in bandgap positions between the TP and SP modes is exhibited by the corresponding modes' R-minimum positions. Hence, the broadening or narrowing of the R-profile indicates the change in the coupling strength. The coupling between the TP and SP modes leads to the repulsion of their dispersion profile, which also depends on the metal layer thickness [23]. Likewise, the excitation of TP-SP hybrid modes depends on the total internal reflection conditions, and thus, these modes are sensitive to the incident light's polarization [1]. The anti-crossing effect alters the hybrid TP-SP plasmonic modes' dispersion properties and decreases the SP mode's absorption losses. Therefore, the hybrid TP-SP system enhances the sensitivity if used as a sensor.

The coupling between the TP and SP modes against the incident light's polarization angle is manifested in the R-profiles shown in Fig. 3. Figure 3 also shows the effects of d_{Ag}. When d_{Ag} = 50 nm, as shown in Fig. 3(a), there is minimal splitting between TP and SP hybrid modes, ~2 nm, at $\varphi = 0$. TP and SP resonance spectra overlap and the modes do not interact with each other significantly. The results are similar when we increase φ. However, increasing φ increases R, which may degrade the sensor performance.

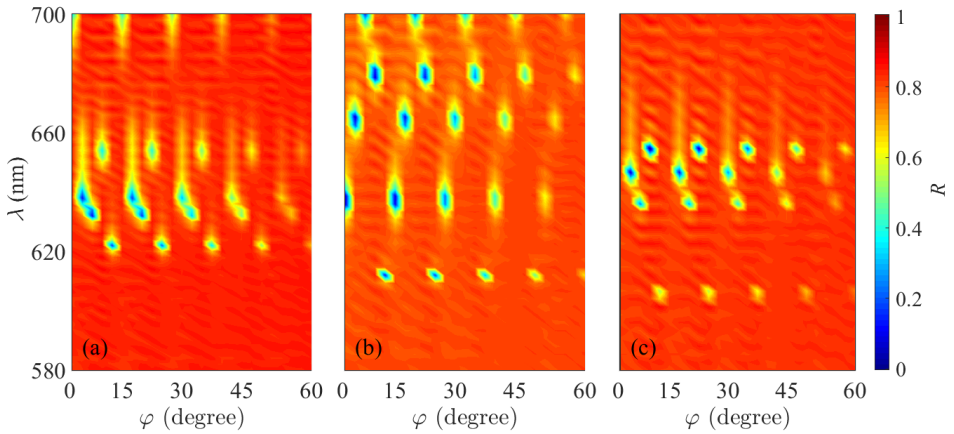

Fig. 3. R-spectra of the proposed sensor vs. polarization angle (φ) when (a) d_{Ag} = 50 nm, (b) d_{Ag} = 60 nm, and (c) d_{Ag} = 70 nm. In each case, n_{Hb} = 1.32919.

Figure 3(b) shows a spectral separation of 30 nm between the TP and SP modes when $\varphi = 0$ and d_{Ag} = 60 nm. Therefore, a minimum gap is observed, which splits the SP mode from the TP mode and moves it far away from the Ag layer. Also, a minimum R value is observed, which indicates a narrower R-profile. Thus, it enhances the sensor performance. However, increasing φ increases R, indicating decreasing incident light absorption on the GPC-based sensor. As a result, the sensor performance decreases. Figure 3(c) shows a spectral separation of 8 nm when $\varphi = 0$ and d_{Ag} = 70 nm. The spectral separation decreases when d_{Ag} increases from 60 to 70 nm. When the Ag layer thickness is >60 nm, SP and TP modes show weak inter-modal interaction [45]. Consequently, using d_{Ag} = 70 nm in the proposed GPC-based sensor reduces the sensor performances. The sensor shows φ-dependence with d_{Ag} = 70 nm as well.

Optics EXPRESS

2.4. Simulation method

In this work, we apply 2-D FDTD simulations to analyze the interaction of the sensor structure with the incident light. The simulation area is 9000×1000 nm^2 in the xy plane. We use the perfectly matched layers (PML) boundary condition in the x-direction while the Bloch boundary condition in the y-direction. We find solutions for a 2-D structure as the proposed sensor structure does not vary in the z direction. We use a non-uniform meshing technique with ultra-fine mesh grids in FDTD simulations to limit the overall error to <0.05%. We have set a high mesh accuracy and used 1000 fs simulation time for the method. For convergence testing, we varied the PML layer number from 8 to 16 and found the minimum reflected light intensity variation of about 0.01% for TP and 0.028% for SP modes.

We used a TM- or TE-polarized light source with a 633 nm wavelength. The light incidence is oblique to enhance absorption by the GPC [46]. We vary the incidence angle from 55° to 70° to determine the R-profile. The light source is placed in the BK7 region at 4250 nm from the BK7-graphene interface. The R value is also recorded in the BK7 region at 4400 nm from the same interface.

3. Theoretical modeling

3.1. Optical properties

The optical properties of different layers of the proposed sensor are dispersive. As a result, the interaction of light with the sensor structure depends on the incident light's wavelength. The 633-nm wavelength of the incident light is often used in experiments [36]. The wavelength-dependent refractive index of the BK7 prism layer is calculated using the following expression [47]

$$n_{\mathrm{BK7}} = \left(\frac{1.03961212\lambda^2}{\lambda^2 - 0.0060006986} + \frac{0.231792344\lambda^2}{\lambda^2 - 0.0200179144} + \frac{1.039612\lambda^2}{\lambda^2 - 103.560653} + 1 \right)^{1/2}. \quad (1)$$

Since graphene is an optically anisotropic uniaxial material due to its 2-D behavior, its permittivity (ε_g) tensor is given by [48]

$$\varepsilon_g = \begin{bmatrix} \varepsilon_{g,t} & 0 & 0 \\ 0 & \varepsilon_{g,t} & 0 \\ 0 & 0 & \varepsilon_{g,n} \end{bmatrix}, \quad (2)$$

where the normal part of the graphene permittivity $\varepsilon_{g,n} = 1$ as the electric field of normal incidence cannot stimulate any current in the graphene sheet. However, the tangential part of the graphene permittivity ($\varepsilon_{g,t}$) is given by [49]

$$\varepsilon_{g,t} = 1 + i\frac{\sigma(\omega)}{\omega\varepsilon_0 t_g}, \quad (3)$$

where $\sigma(\omega)$ is the conductivity of monolayer graphene, ω is the angular frequency of the incident wave, and ε_0 is the permittivity of free space. Monolayer graphene's $\sigma(\omega)$ fundamentally depends on Kubo formula given by [50]

$$\sigma(\omega) = i\frac{e^2 k_B T}{\pi\hbar^2(\omega + i\tau^{-1})}\left[\frac{E_f}{k_B T} + 2\ln\left(\exp\left(-\frac{E_f}{k_B T}\right) + 1\right)\right] + i\frac{e^2}{4\pi\hbar}\ln\left[\frac{2 \mid E_f \mid -\hbar(\omega + i\tau^{-1})}{2 \mid E_f \mid +\hbar(\omega + i\tau^{-1})}\right], \quad (4)$$

where k_B is the Boltzmann constant, E_f is the Fermi energy, e is the electronic charge, T is the temperature, $\hbar$ is the reduced Planck constant, and τ is the relaxation time of carriers. Here, we

Optics EXPRESS

use $E_f = 0.65$ eV, and $T = 300$ K. To model graphene $\sigma(\omega)$, phenomenological scattering rate (Γ) is used in the FDTD-based method. We use $\Gamma = 0.51423$ meV, where $\tau = 1/2\Gamma$.

The dispersion relation of anisotropic graphene can be expressed as [51]

$$k_x^2 + k_y^2 = \varepsilon_{g,t} k_0^2 \quad \text{for (TE)}, \tag{5a}$$

$$\frac{k_x^2}{\varepsilon_{g,t}} + \frac{k_y^2}{\varepsilon_{g,t}} = k_0^2 \quad \text{for (TM)}, \tag{5b}$$

where $k_0 = 2\pi/\lambda$. For TE polarization, $k_{ix} = \sqrt{k_0^2 \varepsilon_i - k_{iy}^2}$, where $k_{iy} = k_y = k_0 \sin\theta_i$ is the tangential part of the wave-vector of each layer related to the incidence light [52], and ε_i is $\varepsilon_{g,n}$, ε_S, and ε_T for graphene, SiO_2, and TiO_2, respectively. For TM polarization, the wave-vector of graphene, SiO_2, and TiO_2 are $k_{gx} = \sqrt{k_0^2 \varepsilon_{g,t} - k_x^2(\varepsilon_{g,t}/\varepsilon_{g,n})}$, $k_{Sx} = \sqrt{k_0^2 \varepsilon_S - k_y^2}$, and $k_{Tx} = \sqrt{k_0^2 \varepsilon_T - k_y^2}$, respectively, where $\varepsilon_{g,n} = 1$. For TE polarization, the R-profile depends on $\varepsilon_{g,t}$ and does not require an obliquely incident light [53]. However, for TM-polarization, the R-profile depends on both $\varepsilon_{g,t}$, and $\varepsilon_{g,n}$ and requires the obliquity of incidence angle. Consequently, the proposed structure shows isotropic behavior for normal incidence. Alternatively, the proposed sensor shows anisotropic behavior due to the obliquity of incident light.

The refractive index of SiO_2 and TiO_2 are 1.45702 and 2.30, respectively [54,55]. The Refractive index of Ag is determined by the Drude-Lorentz model [56]. We use AEC as an antibody made by fibronectin with a refractive index of 1.45 [57]. Human blood refractive index for Hb varies from 1.32919 to 1.36019, and the Hb level grows 6.1025 g/L for every 0.001 RIU variations in blood [33]. Therefore, the refractive index of the blood sample with different Hb levels is determined by Barer's model [58]

$$n_{\text{Hb}} = n_0 + C\Delta\lambda, \tag{6}$$

where n_0 is the reference refractive index, $C = 0.00276\ \text{nm}^{-1}$ is the protein refraction increment constant, and $\Delta\lambda$ is the change of resonance wavelength. The Hb level is related to n_{Hb} by [34]

$$H_r = H_0 + \text{A}\Delta n, \tag{7}$$

where H_0 is the reference Hb level, H_r is the final Hb level, A = 6102.50 is a constant, Δn is the change in refractive index.

3.2. TP and SP resonances

TP modes are electromagnetic waves excited at the interface between a metal and GPC due to consecutive reflections [29]. In our proposed sensor, TP modes are created at the Ag-GPC interface. The dispersion curve of a TP mode lies within the light line, and thus, the TP mode can be excited by both oblique and normal incident light [59]. When TP modes are excited, $R_{\text{M}} R_{\text{GPC}} = 1$, where R_{M} and R_{GPC} are the amplitude reflection coefficients of metal and GPC, respectively [60]. Notably, $R_{\text{M}}, R_{\text{GPC}} \simeq -1$ at the visible wavelength range [29]. Therefore, TP modes are confined between Ag, which has a negative real permittivity, and GPC bandgap. As light is incident on the sensor from the GPC side, as shown in Fig. 1, the energy confinement in TP modes will create a dip in the R-profile [60]. In addition, in such a GPC-based structure where Ag is present, TP and SP modes cannot be excited separately at a specific incidence angle [23]. There is a superposition of electromagnetic waves localized at the Ag-GPC interface due to TP and at the Ag-sensing layer interface due to SP, creating a hybrid state.

In Fig. 4, we show the R-profile of the proposed sensor structure when $n_{\text{Hb}} = 1.32919$, $N = 9$, and $\varphi = 0°$. We note two distinct R minima. The first dip at 57.52° is due to the excitation of

Optics EXPRESS

TP between Ag and GPC, whereas the second dip at 63.96° is due to the excitation of SP at the Ag-sensing layer interface. The FWHM due to TP is 0.1708°, whereas it is 0.4730° due to the excitation of SP. In addition, several ripples in the *R*-profile are due to weak photonic modes excited in the various GPC layers.

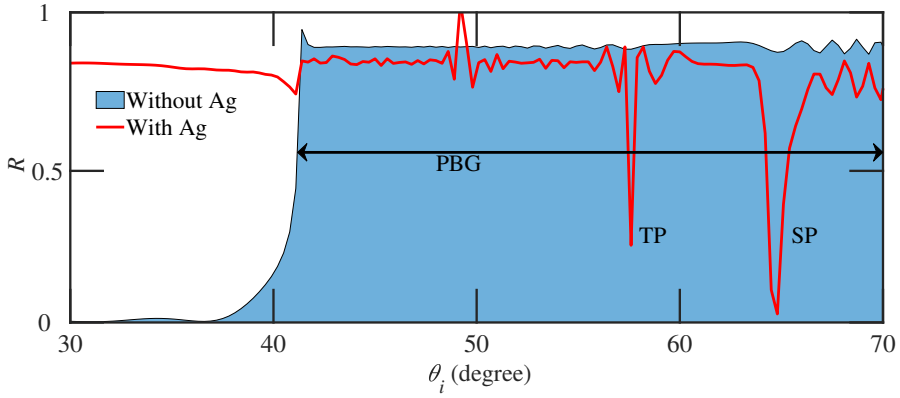

Fig. 4. *R*-profile of the proposed sensor with and without the Ag layer, when $N = 9$, $\lambda = 633$ nm, $n_{\mathrm{Hb}} = 1.32919$, and $d_{\mathrm{Ag}} = 60$ nm. The dips in the solid red line at 57.52° and 63.96° within the PBG represent TP and SP resonance modes, respectively.

In Fig. 4, we show *R*-profile with and without the Ag layer. In the first case, we simulate the sensor without the Ag layer, i.e., the BK7-GPC-Sensing layer structure, to determine PBG [61]. The sensor without Ag shows a PBG when θ_i varies from 41.1° to 60°, with no excited mode in this region. Next, we simulate the sensor with the Ag layer, i.e., the BK7-GPCs-Ag-Graphene-Antibody-Sensing layer structure. We observe a resonance dip at 57.52°. This resonance is a TP mode located inside the PBG, created by the interference of electromagnetic waves at the interface between Ag and GPC layers [31].

3.3. Coupling energy to TP and SP modes

FMSA approach permits the examination of each mode's characteristics, including spatial energy density profile and uncoupling of different scattering [62]. We follow the approach of Ref. [63] to determine how strongly energy couples to a particular mode and shifts from TP to SP modes. Using the FMSA method helps us to analyze the energy coupled to each mode separately. One-dimensional (1-D) fast Fourier transform (FFT) is performed on the coupled light to the sensor to find the wave vector or spatial frequency. Figures 5(a)-(c) presents a Fourier power profile vs. spatial frequency for different N. In addition, we present the same analysis when φ changes to observe the φ-dependent energy coupling from TP to SP in Figs. 5(d)-(f).

The first mode at 0.0173 $\mu\mathrm{m}^{-1}$ in Fig. 5(a) represents the TP mode, whereas the second mode at 0.7983 $\mu\mathrm{m}^{-1}$ represents the SP mode. We have also calculated the spatial frequency for SP modes using $k_{\mathrm{SP}} = k_0\sqrt{\varepsilon_m\varepsilon_{\mathrm{Hb}}/(\varepsilon_m + \varepsilon_{\mathrm{Hb}})}$ and for TP modes using $k_{\mathrm{TP}} = k_0\sqrt{\varepsilon_m\varepsilon_{\mathrm{eff}}/(\varepsilon_m + \varepsilon_{\mathrm{eff}})}$, where ε_m is the real part of the permittivity of Ag and $\varepsilon_{\mathrm{eff}}$ is the effective permittivity of GPC. In Figs. 5(a) and (b), when $N = 5$ and 7, maximum power is coupled to the sensor with the TP mode confining greater power than the SP mode. When N increases from 7 to 9, the TP mode's power decreases, with both modes confining power approximately equally, making the coupled energy transfer from the TP mode to the SP mode when N increases.

Figures 5(d)–(f) show that the coupled power to TP and SP modes decreases as φ increases, however, with power confining more to the SP mode than the TP mode. We aim to couple energy from TP to SP in the proposed sensor. As the maximum energy of TPs is confined in the GPC

Optics EXPRESS

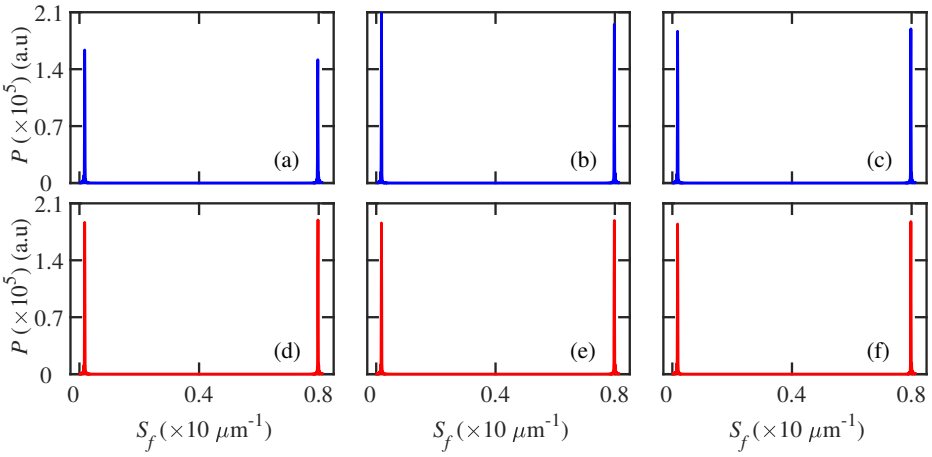

Fig. 5. Fourier power spectrum vs. spatial frequency for (a) $N = 5$, (b) $N = 7$, and (c) $N = 9$, when $\varphi = 0$, and (d) $\varphi = 0$, (e) $\varphi = 30°$, and (f) $\varphi = 60°$, when $N = 9$. In each case, $n_{\mathrm{Hb}} = 1.32919$ and $d_{\mathrm{Ag}} = 60$ nm.

and near the Ag-GPC interface, TP electromagnetic fields barely relate to the outer sensor surface. Therefore, the TP mode features are less responsive to the changes of the refractive index of sensing medium [25].

3.4. Sensor performance parameters

Sensitivity (S) and FoM are the main performance parameters of GPC-based TP-SP hybrid resonance sensors. These parameters are determined using the R-profile. The sensitivity is determined as [64]

$$S_{\mathrm{SP/TP}} = \frac{\Delta\theta_r(\mathrm{SP/TP})}{\Delta n_{\mathrm{Hb}}}, \tag{8}$$

where $\Delta\theta_r$(SP/TP) is the change in resonance angle of θ_r for either SP or TP mode. On the other hand, FoM is determined as [65]

$$\mathrm{FoM}_{\mathrm{SP/TP}} = \frac{S_{\mathrm{SP/TP}}}{\mathrm{FWHM}_{\mathrm{SP/TP}}}. \tag{9}$$

4. Sensing performance

Figure 6(a) shows the sensing layer refractive index as a function of C_{Hb}. We vary C_{Hb} from zero to 189 g/L. The sensing layer refractive index n_{Hb}, in the presence of Hb, is calculated using Eqs. (7) and (8). When $C_{\mathrm{Hb}} = 0$, $n_{\mathrm{Hb}} = 1.32919$, and n_{Hb} linearly increases to 1.36019 as C_{Hb} increases to 189 g/L. As C_{Hb} changes in the human blood sample, the sensing layer experiences a difference in n_{Hb}. Consequently, the index variation changes SP and TP wave vectors, ultimately changing the resonance angle θ_r for TP and SP modes.

Figure 6(b) shows $\Delta\theta_r$ for the TP mode as a function of the C_{Hb} level for different φ. We note that $\Delta\theta_r$ increases with C_{Hb} for the TP mode. However, $\Delta\theta_r$ does not vary noticeably when φ changes from 0° to 30°. When φ changes from 0° to 60°, the change in $\Delta\theta_r$ is significant. Figure 6(c) shows a similar trend in the $\Delta\theta_r$ vs. C_{Hb} relationship for the SP mode. However, $\Delta\theta_r$ changes more significantly for the SP mode than the TP mode. We note that $\Delta\theta_r$ for the SP mode is ~2 times greater than $\Delta\theta_r$ for the TP mode.

Figure 7 shows the sensor performances as a function of C_{Hb} using the TP resonance separately. Figure 7 also shows the polarization-dependent anisotropic behavior of the proposed sensor. We

Optics EXPRESS

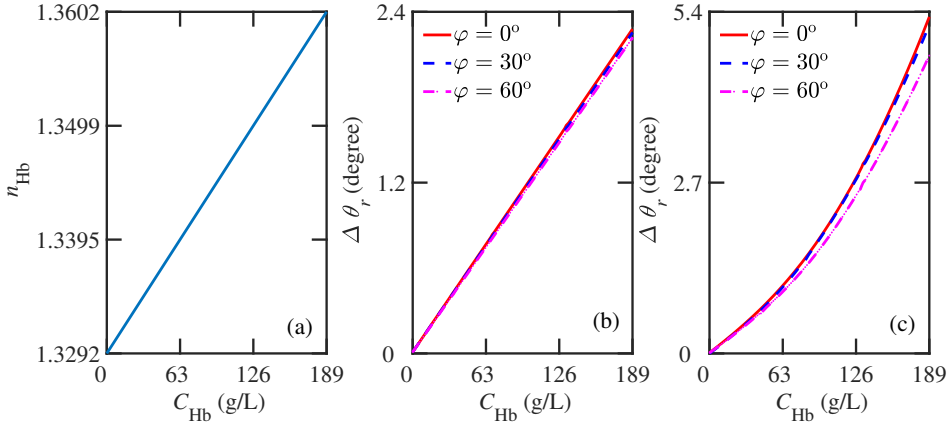

Fig. 6. (a) Sensing layer refractive index vs. Hb concentration (C_{Hb}), (b) $\Delta\theta_r$ vs. C_{Hb} for the TP resonance mode, and (c) $\Delta\theta_r$ vs. C_{Hb} for the SP resonance mode.

use $\varphi = 0$, 30°, and 60°, where $\varphi = 0$ means that the incident light is TM polarized, whereas $\varphi = 30°$ and 60° represent the TE-polarized incident light. Figure 7(a) shows the sensitivity of the proposed sensor as a function of C_{Hb}. Considering the TP mode, the sensitivity increases slightly and depends on C_{Hb} negligibly. Since the energy of the excited TP mode is confined at the Ag-GPC interface, the electromagnetic field due to the TP mode insignificantly interacts with the sensing layer. Hence, $\Delta\theta_r$ is linear for the TP mode and increases approximately at a constant rate, as shown in Fig. 6(b). Therefore, the sensitivity is approximately constant for a C_{Hb} from 0 to 189 g/L. The maximum sensitivity is observed at $\varphi = 0$, and the sensitivity decreases when φ increases since $\Delta\theta_r$ reduces gradually as φ increases, as shown in Fig. 6(b). Therefore, we note that the TP mode shows low polarization-dependent sensitivity.

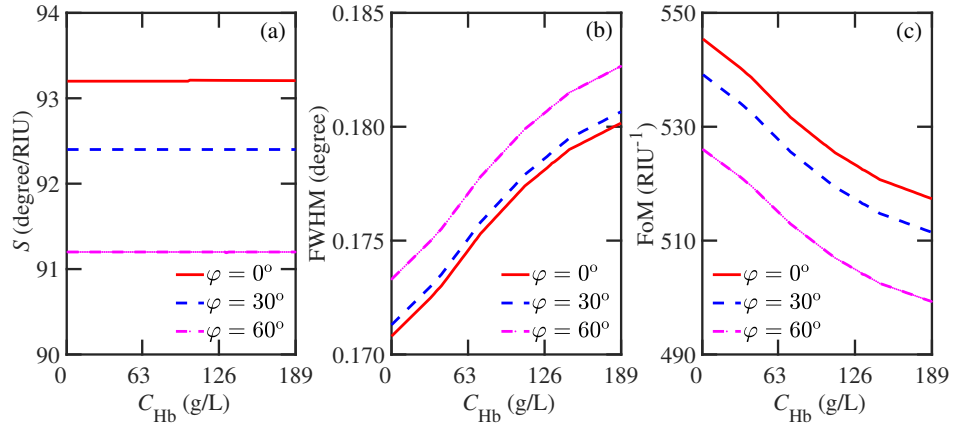

Fig. 7. (a) S, (b) FWHM, and (c) FoM as a function of C_{Hb} of the proposed GPCs-based sensor using TPs resonance mode.

Figure 7(b) shows the FWHM of the proposed sensor as a function of C_{Hb} for different φ for TP resonances. The FWHM increases when C_{Hb} or φ increases since the R-profile broadens when C_{Hb} or φ increases. In Fig. 7(c), we show the FoM of the proposed sensor for the TP mode. Generally, FoM decreases when C_{Hb} or φ increases. However, when $\varphi = 0$ and C_{Hb} is zero, the FoM is maximum with a value of 545 RIU^{-1}. The value of FoM gradually decreases when C_{Hb}

Optics EXPRESS

increases and FoM = 517 RIU^{-1} when C_{Hb} is 189 g/L. As the increasing C_{Hb} raises the n_{Hb} value, $\Delta\theta_r$ increases. However, the FWHM increases as C_{Hb} increases, and hence decreasing FoM. Similar tendency is observed when $\varphi = 30°$ and $\varphi = 60°$. However, FoM decrease more when $\varphi = 60°$ than when $\varphi = 30°$. Therefore, the proposed GPC-based sensor shows performances that depend on the polarization of the incident light.

Figure 8(a) shows the sensitivity of the proposed sensor as a function of C_{Hb} considering the SP mode. The sensitivity increases significantly as a function of C_{Hb} due to a large resonance angle shift. As energy confines in the Ag-sensing layer interface due to the SP resonance, the electromagnetic field interacts significantly with the sensing element. The sensitivity increases from 138 to 220 degrees/RIU when C_{Hb} increases from zero to 189 g/L. At C_{Hb} = 189 g/L, the sensitivity using the SP mode is 57.60% greater than the TP mode. However, the sensitivity decreases with φ and decreases maximum when $\varphi = 60°$. We note that when C_{Hb} is 189 g/L, the sensitivity decreases from 220 to 181 degrees/RIU as φ increases from 0 to 60°. Thus, the proposed sensor's sensitivity depends on the incident light's polarization.

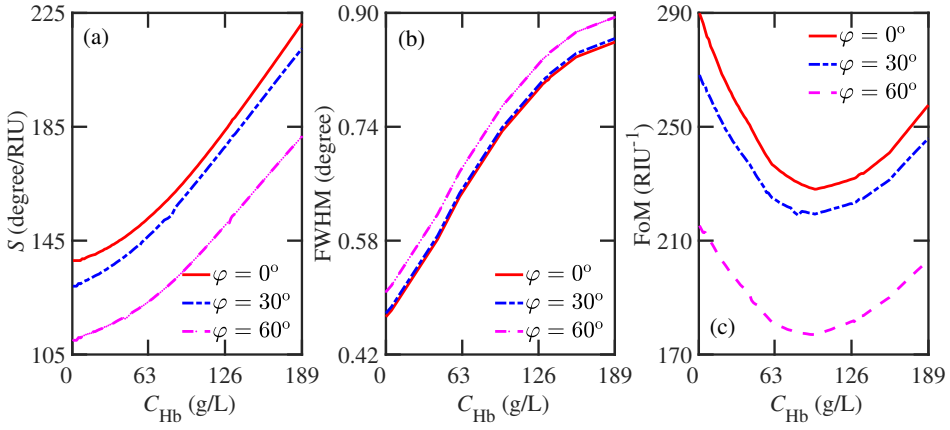

Fig. 8. (a) S, (b) FWHM, and (c) FoM as a function of C_{Hb} of the proposed GPCs-based sensor using SPs resonance mode.

Figure 8(b) shows the FWHM of the proposed sensor for the SP mode as a function of C_{Hb} for different φ. The FWHM increases when C_{Hb} or φ increases. The FWHM increases by approximately three times the TP mode as the R-profile of SP resonances is much broader than TP resonances when C_{Hb} or φ increases. The main reason for the broader FWHM of the SP mode is the losses associated with the Ag layer, which is essential for the plasmonic wave creation [1]. In Fig. 8(c), we show the FoM of the proposed sensor for the SP mode. Generally, FoM decreases when C_{Hb} increases from zero to 100 g/L. After that, it starts to increase. This tendency is observed for all the values of φ. Similar to the trend observed for the sensitivity, the FoM decreases more significantly when $\varphi = 60°$.

However, when $\varphi = 0$ and $C_{Hb} = 0$, the FoM is maximum with a value of 290 RIU^{-1}. If we use the SP mode instead of the TP mode, FoM reduces by 46.77% when $\varphi = 0$. FoM gradually decreases when C_{Hb} increases and FoM = 228 RIU^{-1} when C_{Hb} = 100 g/L. As n_{Hb} increases with C_{Hb}, $\Delta\theta_r$ also increases. However, the FWHM increases as C_{Hb} increases, decreasing FoM. A similar tendency is observed when $\varphi = 30°$ and 60°. FoM increases for C_{Hb}>100 g/L as FWHM gradually saturates when C_{Hb}>100 g/L, as shown in Fig. 8(b). The SP mode shows a significant dependence of its performance on the polarization of the incident light.

In a hybrid TP-SP mode, the TP mode drives the SP mode away from the Ag layer, decreasing the loss associated with the SP mode. In TP resonance, the FWHM is narrower due to low losses,

Optics EXPRESS

as only a part of the TP mode propagates at the Ag-GPC interface, offering higher FoM. However, the TP mode is excited at the inner side of the Ag layer; hence, does not directly access the sensing element [1]. Consequently, using the hybrid TP-SP mode for biosensing explores the TP mode in a strong coupling region, and applying one more mode provides the accuracy of sensing performances [5]. We can control the width of the *R*-profile by transferring the TP mode energy to the SP mode, helping the SP mode provide the minimum *R* value with a narrower FWHM.

Next, we calculate the sensitivity and FoM using DDM to hybrid TP-SP modes in the proposed sensor. The sensitivity is calculated as [66,67]

$$S_{\mathrm{DDM}} = \frac{\Delta\theta_{\mathrm{SP}}}{\Delta n_{\mathrm{Hb}}} + \frac{\Delta\theta_{\mathrm{TP}}}{\Delta n_{\mathrm{Hb}}}, \tag{10}$$

where $\Delta\theta_{\mathrm{SP}}$ and $\Delta\theta_{\mathrm{TP}}$ are the changes in resonance angles of SP and TP resonance modes, respectively. In addition, we determine the FoM as [66]

$$\mathrm{FoM} = S_{\mathrm{DDM}}/\mathrm{FWHM}_{\mathrm{SP/TP}}, \tag{11}$$

where $\mathrm{FWHM}_{\mathrm{SP/TP}}$ is FWHM for either SP or TP resonance mode. In DDM, $\mathrm{FWHM}_{\mathrm{SP}}$ is usually used for FoM calculation. In Fig. 9(a), we show the sensitivity of the proposed GPC-based sensor as a function of C_{Hb} for different φ using DDM. The sensitivity increases when C_{Hb} increases but decreases when φ increases. When C_{Hb} is 189 g/L, sensitivity is maximum, i.e., 314.5 degrees/RIU. The sensitivity obtained using DDM increases by ~30% when compared with that obtained using only the SP mode. The sensitivity decreases with φ, showing polarization-dependent characteristics using DDM.

Figure 9(b) shows the FoM determined using the TP mode. The FoM is considerably high, ~1740 RIU^{-1}, for $\varphi = 0$ and $C_{\mathrm{Hb}} = 189$ g/L. The TP resonance provides a narrow FWHM due to a small loss of incident light at the Ag-GPC interface. The FoM using the TP mode also shows a polarization-dependent behavior. Figure 9(c) also shows the FoM of the proposed sensor for the SP resonance mode. Generally, FoM decreases when C_{Hb} increases from zero to 126 g/L and then increases for C_{HB}>126 g/L. This tendency is observed for all φ. As usual, the FoM reduction rate in the sensitivity analysis is more severe when $\varphi = 60°$. Compared to the SP resonance mode, when $\varphi = 0$ and $C_{\mathrm{Hb}} = 0$, the FoM enhancement is ~40% using DDM. Using the SP mode, FoM progressively decreases at a C_{Hb} is around 100 g/L, as shown in Fig. 8(c). However, using DDM, this position shifts to 126 g/L as DDM offers more sensitivity enhancement.

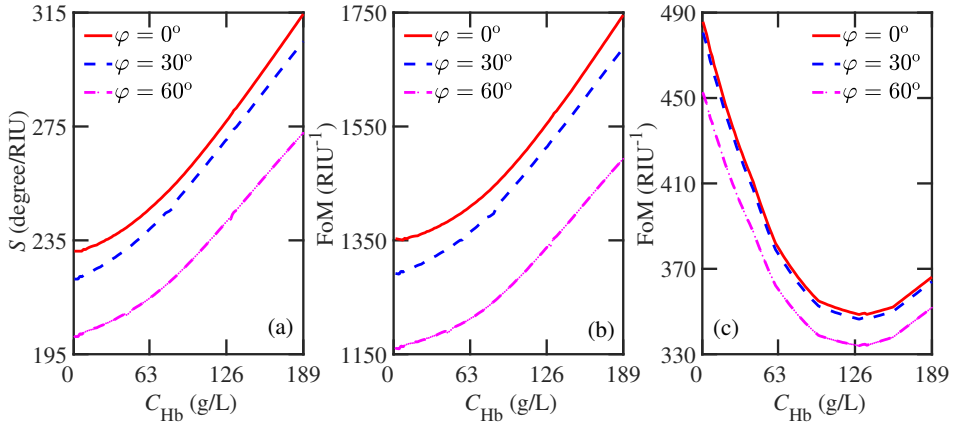

Fig. 9. (a) *S*, (b) FoM using TPs, and (c) FoM using SPs as a function of C_{Hb} of the proposed GPCs-based sensor applying DDM.

Optics EXPRESS

The proposed GPC-based sensor's sensitivity and FoM are better than the state-of-the-art optical sensors. We compare the sensitivity and FoM of the proposed sensor in Table 1 with some recently reported sensors. C_{Hb} is 189 g/L, which corresponds to n_{Hb} = 1.36019 with those reported in the literature, as given in Table 1. The compared sensors also operate at 633 nm incident wavelength and report results for a sample of index ~1.36. We have considered whether or not the sensor uses the DDM technique to determine the sensitivity and FoM.

Table 1. Performance comparison of our proposed sensor with different recently proposed sensors with or without using DDM.

Sensor configuration	S (degree/RIU)	FoM (RIU^{-1})
Metal grating-based (DDM) [67]	237	138
Graphene-based hybrid TP [7]	–	161
2-D materials based SPR [68]	235	71
2-D materials ($PtSe_2$) based SPR [69]	162	15
Two DBRs hybrid TP-SP [25]	–	12
Graphene-based SPR for Hb detection [34]	200	–
This work (TP)	93	545
This work (SP)	189	290
This work (DDM, SP)	314.5	486
This work (DDM, TP)	314.5	1746

5. Conclusion

The proposed anisotropic GPC-based hybrid SP-TP mode sensor can sense the Hb level in a blood sample with high sensitivity and FoM. We find that the sensor performances depend on the hybrid plasmonic mode, which can be controlled through the energy coupling between TP and SP modes with an appropriate Ag layer thickness. This mode coupling decreases losses incurred in the Ag layer and narrows the plasmonic resonances. We utilize the anisotropic properties of the GPC and observe polarization-dependent sensor performance. Using DDM, a maximum of 314.5 degree/RIU sensitivity and 1746 RIU^{-1} FoM are found when C_{Hb} is 189 g/L. Besides, we can employ the TP resonance mode as a secondary probe, which can provide extra information for analyzing the adsorption process at different interfaces of metal-GPC structure. The proposed TP-SP hybrid modes of the GPC-based sensors can be used for various types of protein detection.

Disclosures. The authors declare that they have no conflict of interest.

Data Availability. Data underlying the results presented in this paper are not publicly available at this time but may be obtained from the authors upon reasonable request.

References

1. E. Buzavaite-Verteliene, I. Plikusiene, T. Tolenis, *et al.*, "Hybrid tamm-surface plasmon polariton mode for highly sensitive detection of protein interactions," Opt. Express **28**(20), 29033–29043 (2020).
2. M. Baitimirova, R. Viter, J. Andzane, *et al.*, "Tuning of structural and optical properties of graphene/zno nanolaminates," J. Phys. Chem. C **120**(41), 23716–23725 (2016).
3. M. S. Rahman, M. R. Hasan, K. A. Rikta, *et al.*, "A novel graphene coated surface plasmon resonance biosensor with tungsten disulfide (ws2) for sensing dna hybridization," Opt. Mater. **75**, 567–573 (2018).
4. P. Cao, X. Yang, S. Wang, *et al.*, "Ultrastrong graphene absorption induced by one-dimensional parity-time symmetric photonic crystal," IEEE Photonics J. **9**(1), 1–9 (2017).
5. E. Buzavaite-Verteliene, A. Valavicius, L. Grineviciute, *et al.*, "Influence of the graphene layer on the strong coupling in the hybrid tamm-plasmon polariton mode," Opt. Express **28**(7), 10308–10319 (2020).
6. J. Hu, E. Yao, W. Xie, *et al.*, "Strong longitudinal coupling of tamm plasmon polaritons in graphene/dbr/ag hybrid structure," Opt. Express **27**(13), 18642–18652 (2019).

Optics EXPRESS

7. J. Hu, Y. Huang, Y. Chen, *et al.*, "High-sensitivity multi-channel refractive-index sensor based on a graphene-based hybrid tamm plasmonic structure," Opt. Mater. Express **11**(11), 3833–3843 (2021).
8. Z. Lan, J. W. You, and N. C. Panoiu, "Nonlinear one-way edge-mode interactions for frequency mixing in topological photonic crystals," Phys. Rev. B **101**(15), 155422 (2020).
9. K. V. Sreekanth, S. Zeng, J. Shang, *et al.*, "Excitation of surface electromagnetic waves in a graphene-based bragg grating," Sci. Rep. **2**(1), 737 (2012).
10. F. Al-Sheqefi and W. Belhadj, "Photonic band gap characteristics of one-dimensional graphene-dielectric periodic structures," Superlattices Microstruct. **88**, 127–138 (2015).
11. A. H. Aly and Z. A. Zaky, "Ultra-sensitive photonic crystal cancer cells sensor with a high-quality factor," Cryogenics **104**, 102991 (2019).
12. A. H. Aly and H. A. Elsayed, "Transmittance properties of one-dimensional metallic-dielectric photonic crystals in near-zero permittivity," Phys. Scr. **94**(12), 125501 (2019).
13. L. Qi and C. Liu, "Complex band structures of 1d anisotropic graphene photonic crystal," Photonics Res. **5**(6), 543–551 (2017).
14. C. Qin, B. Wang, H. Huang, *et al.*, "Low-loss plasmonic supermodes in graphene multilayers," Opt. Express **22**(21), 25324–25332 (2014).
15. H. Hajian, H. Caglayan, and E. Ozbay, "Long-range tamm surface plasmons supported by graphene-dielectric metamaterials," J. Appl. Phys. **121**(3), 033101 (2017).
16. Y. Xiang, X. Dai, J. Guo, *et al.*, "Critical coupling with graphene-based hyperbolic metamaterials," Sci. Rep. **4**(1), 5483 (2014).
17. A. A. Sayem, M. Rahman, M. Mahdy, *et al.*, "Negative refraction with superior transmission in graphene-hexagonal boron nitride (hbn) multilayer hyper crystal," Sci. Rep. **6**(1), 25442 (2016).
18. C. Kar, S. Jena, D. V. Udupa, *et al.*, "Tamm plasmon polariton in planar structures: A brief overview and applications," Opt. Laser Technol. **159**, 108928 (2023).
19. T. Qiao, M. Hu, X. Jiang, *et al.*, "Generation and tunability of supermodes in tamm plasmon topological superlattices," ACS Photonics **8**(7), 2095–2102 (2021).
20. B. Du, H. Lu, L. Zhang, *et al.*, "Fiber-integrated tamm plasmon polariton system," J. Lightwave Technol. **40**(15), 5280–5285 (2022).
21. X. Wang, X. Jiang, Q. You, *et al.*, "Tunable and multichannel terahertz perfect absorber due to tamm surface plasmons with graphene," Photonics Res. **5**(6), 536–542 (2017).
22. B. Roy, S. Majumder, and R. Chakraborty, "Design of low loss surface plasmon polariton waveguide and its use as hybrid tamm sensor with improved sensitivity," Opt. Eng. **59**(01), 1 (2020).
23. B. Afinogenov, V. Bessonov, A. Nikulin, *et al.*, "Observation of hybrid state of tamm and surface plasmon-polaritons in one-dimensional photonic crystals," Appl. Phys. Lett. **103**(6), 061112 (2013).
24. P. Torma and W. L. Barnes, "Strong coupling between surface plasmon polaritons and emitters: a review," Rep. Prog. Phys. **78**(1), 013901 (2014).
25. S. Kumar, M. K. Shukla, P. S. Maji, *et al.*, "Self-referenced refractive index sensing with hybrid-tamm-plasmon-polariton modes in sub-wavelength analyte layers," J. Phys. D: Appl. Phys. **50**(37), 375106 (2017).
26. P. S. Maji, M. K. Shukla, and R. Das, "Blood component detection based on miniaturized self-referenced hybrid tamm-plasmon-polariton sensor," Sens. Actuators, B **255**, 729–734 (2018).
27. Z. A. Zaky and A. H. Aly, "Modeling of a biosensor using tamm resonance excited by graphene," Appl. Opt. **60**(5), 1411–1419 (2021).
28. H. Su, T. Jiang, R. Zhou, *et al.*, "High-sensitivity terahertz sensor based on tamm plasmon polaritons of a graphene asymmetric structure," J. Opt. Soc. Am. B **38**(6), 1877–1884 (2021).
29. M. M. Keshavarz and A. Alighanbari, "Terahertz refractive index sensor based on tamm plasmon-polaritons with graphene," Appl. Opt. **58**(13), 3604–3612 (2019).
30. S. Shi, S. Yuan, J. Zhou, *et al.*, "Terahertz technology and its applications in head and neck diseases," iScience **26**(7), 107060 (2023).
31. A. M. Ahmed and A. Mehaney, "Ultra-high sensitive 1d porous silicon photonic crystal sensor based on the coupling of tamm/fano resonances in the mid-infrared region," Sci. Rep. **9**(1), 6973 (2019).
32. D. T. Gilbertson, J. P. Ebben, R. N. Foley, *et al.*, "Hemoglobin level variability: associations with mortality," Clin. J. Am. Soc. Nephrol. **3**(1), 133–138 (2008).
33. A. K. Ajad, M. J. Islam, M. R. Kaysir, *et al.*, "Highly sensitive bio sensor based on wgm ring resonator for hemoglobin detection in blood samples," Optik **226**, 166009 (2021).
34. S. Mostufa, A. K. Paul, and K. Chakrabarti, "Detection of hemoglobin in blood and urine glucose level samples using a graphene-coated spr based biosensor," OSA Continuum **4**(8), 2164–2176 (2021).
35. T. Huang, X. Dang, L. Han, *et al.*, "Dual-channel sensor based on tamm plasmon polariton and defect mode hybridization in topological insulator covered photonic crystals," J. Opt. Soc. Am. B **38**(6), 1951–1957 (2021).
36. G. Lan, S. Liu, Y. Ma, *et al.*, "Sensitivity and figure-of-merit enhancements of liquid-prism spr sensor in the angular interrogation," Opt. Commun. **352**, 49–54 (2015).
37. F. Ramos-Mendieta and P. Halevi, "Propagation constant-limited surface modes in dielectric superlattices," Opt. Commun. **129**(1-2), 1–5 (1996).

Optics EXPRESS

38. D. H. Kim, H. G. Oh, W. H. Park, *et al.*, "Detection of alpha-fetoprotein in hepatocellular carcinoma patient plasma with graphene field-effect transistor," Sensors **18**(11), 4032 (2018).
39. D. Miura, H. Kimura, W. Tsugawa, *et al.*, "Rapid, convenient, and highly sensitive detection of human hemoglobin in serum using a high-affinity bivalent antibody–enzyme complex," Talanta **234**, 122638 (2021).
40. A. Panda, P. D. Pukhrambam, and G. Keiser, "Performance analysis of graphene-based surface plasmon resonance biosensor for blood glucose and gas detection," Appl. Phys. A **126**(3), 153 (2020).
41. C.-W. Lin, K.-P. Chen, C.-N. Hsiao, *et al.*, "Design and fabrication of an alternating dielectric multi-layer device for surface plasmon resonance sensor," Sens. Actuators, B **113**(1), 169–176 (2006).
42. R. Nasirifar, M. Danaie, and A. Dideban, "Dual channel optical fiber refractive index sensor based on surface plasmon resonance," Optik **186**, 194–204 (2019).
43. M. H. Elshorbagy, A. Cuadrado, and J. Alda, "High-sensitivity integrated devices based on surface plasmon resonance for sensing applications," Photonics Res. **5**(6), 654–661 (2017).
44. S. Azzini, G. Lheureux, C. Symonds, *et al.*, "Generation and spatial control of hybrid tamm plasmon/surface plasmon modes," ACS Photonics **3**(10), 1776–1781 (2016).
45. R. Das, T. Srivastava, and R. Jha, "On the performance of tamm-plasmon and surface-plasmon hybrid-mode refractive-index sensor in metallo-dielectric heterostructure configuration," Sens. Actuators, B **206**, 443–448 (2015).
46. J.-T. Liu, N.-H. Liu, J. Li, *et al.*, "Enhanced absorption of graphene with one-dimensional photonic crystal," Appl. Phys. Lett. **101**(5), 052104 (2012).
47. P. Sun, M. Wang, L. Liu, *et al.*, "Sensitivity enhancement of surface plasmon resonance biosensor based on graphene and barium titanate layers," Appl. Surf. Sci. **475**, 342–347 (2019).
48. B. Zhu, G. Ren, S. Zheng, *et al.*, "Nanoscale dielectric-graphene-dielectric tunable infrared waveguide with ultrahigh refractive indices," Opt. Express **21**(14), 17089–17096 (2013).
49. G.-W. Ding, S.-B. Liu, H.-F. Zhang, *et al.*, "Tunable electromagnetically induced transparency at terahertz frequencies in coupled graphene metamaterial," Chin. Phys. B **24**(11), 118103 (2015).
50. Q. Bao, H. Zhang, B. Wang, *et al.*, "Broadband graphene polarizer," Nat. Photonics **5**(7), 411–415 (2011).
51. Y. Li, L. Qi, J. Yu, *et al.*, "One-dimensional multiband terahertz graphene photonic crystal filters," Opt. Mater. Express **7**(4), 1228–1239 (2017).
52. L. Hu and S. Chui, "Characteristics of electromagnetic wave propagation in uniaxially anisotropic left-handed materials," Phys. Rev. B **66**(8), 085108 (2002).
53. Z. Saleki, A. Majarshin, Y.-A. Luo, *et al.*, "Spectral statistics of a 1d photonic crystal containing an anisotropic graphene-based hyperbolic metamaterial defect layer," Opt. Mater. **121**, 111483 (2021).
54. H. Philipp, "Silicon dioxide (sio2)(glass)," in *Handbook of Optical Constants of Solids*, (Elsevier, 1997), pp. 749–763.
55. I. Iatsunskyi, E. Coy, R. Viter, *et al.*, "Study on structural, mechanical, and optical properties of al2o3–tio2 nanolaminates prepared by atomic layer deposition," J. Phys. Chem. C **119**(35), 20591–20599 (2015).
56. P. K. Maharana, T. Srivastava, and R. Jha, "On the performance of highly sensitive and accurate graphene-on-aluminum and silicon-based spr biosensor for visible and near infrared," Plasmonics **9**(5), 1113–1120 (2014).
57. A. W. Peterson, M. Halter, A. Tona, *et al.*, "Surface plasmon resonance imaging of cells and surface-associated fibronectin," BMC Cell Biol. **10**(1), 16–17 (2009).
58. W. Bogaerts, P. De Heyn, T. Van Vaerenbergh, *et al.*, "Silicon microring resonators," Laser Photonics Rev. **6**(1), 47–73 (2012).
59. S. Kumar, P. S. Maji, and R. Das, "Tamm-plasmon resonance based temperature sensor in a ta2o5/sio2 based distributed bragg reflector," Sens. Actuators, A **260**, 10–15 (2017).
60. M. Kaliteevski, I. Iorsh, S. Brand, *et al.*, "Tamm plasmon-polaritons: Possible electromagnetic states at the interface of a metal and a dielectric bragg mirror," Phys. Rev. B **76**(16), 165415 (2007).
61. B. Auguie, M. C. Fuertes, P. C. Angelome, *et al.*, "Tamm plasmon resonance in mesoporous multilayers: toward a sensing application," ACS Photonics **1**(9), 775–780 (2014).
62. V. Ferry, "Light trapping in plasmonic solar cells," Ph.D. thesis, Ph. D. thesis, California Institute of Technology, 2011. (2011).
63. A.-L. Baudrion, F. de Leon-Perez, O. Mahboub, *et al.*, "Coupling efficiency of light to surface plasmon polariton for single subwavelength holes in a gold film," Opt. Express **16**(5), 3420–3429 (2008).
64. B. Lahiri, S. G. McMeekin, M. Richard, *et al.*, "Enhanced fano resonance of organic material films deposited on arrays of asymmetric split-ring resonators (a-srrs)," Opt. Express **21**(8), 9343–9352 (2013).
65. M. Hossain and M. A. Talukder, "Optical magnetism in surface plasmon resonance–based sensors for enhanced performance," Plasmonics **16**(2), 581–588 (2021).
66. M. Zhao, J. Wang, Y. Zhang, *et al.*, "Self-referenced refractive index sensor based on double-dips method with bimetal-dielectric and double-groove grating," Opt. Express **30**(5), 8376–8390 (2022).
67. D. Cai, Y. Lu, K. Lin, *et al.*, "Improving the sensitivity of spr sensors based on gratings by double-dips method (ddm)," Opt. Express **16**(19), 14597–14602 (2008).
68. A. Kumar, A. K. Yadav, A. S. Kushwaha, *et al.*, "A comparative study among ws2, mos2 and graphene based surface plasmon resonance (spr) sensor," Sensors and Actuators Reports **2**(1), 100015 (2020).
69. Y. Jia, Z. Li, H. Wang, *et al.*, "Sensitivity enhancement of a surface plasmon resonance sensor with platinum diselenide," Sensors **20**(1), 131 (2019).